



ELSEVIER

Contents lists available at ScienceDirect

Additive Manufacturing

journal homepage: www.elsevier.com/locate/addma

Full Length Article

Influence of processing and microstructure on the local and bulk thermal conductivity of selective laser melted 316L stainless steel

Jacob C. Simmons^a, Xiaobo Chen^a, Arad Azizi^a, Matthias A. Daeumer^a, Peter Y. Zavalij^b, Guangwen Zhou^a, Scott N. Schiffres^{a,*}^a Department of Mechanical Engineering, Binghamton University, Binghamton, NY 13902, United States^b Department of Chemistry and Biochemistry, University of Maryland, College Park, MD 20742, United States

ARTICLE INFO

Keywords:

Thermal conductivity
 Selective laser melting (SLM)
 Additive manufacturing
 316L stainless steel
 Process parameter

ABSTRACT

Material properties of parts made via selective laser melting are not the same as the well-established properties for bulk base materials, due to the unique processes used to produce the parts. Meanwhile, additive manufacturing is increasingly being used for heat exchangers and heat removal devices, which demand high thermal conductivities. The thermal properties are also important for many non-destructive testing technologies. The thermal conductivity of selective laser melted 316L stainless steel was studied as a function of processing conditions and build orientation. The porosity and thermal conductivity were measured versus processing conditions. A critical energy density of 44.4 J/mm³ was observed below which the porosity increased and the thermal conductivity decreased. For the lowest-porosity sample, the local thermal conductivity map taken with frequency domain thermorefectance showed a variation in the stainless steel thermal conductivity between 10.4 and 19.8 W/m-K, while the average thermal conductivity of 14.3 W/m-K from the thermal conductivity map agreed, within measurement uncertainty, with the bulk thermal conductivity measurements. The thermal conductivity trend was not fully explained by the porosity, as effective medium models fail to predict the trend. Amorphous stripes in the selective laser melted stainless steel grains were identified by transmission electron microscopy. These amorphous regions also resulted in decreased x-ray diffraction intensities with increasing porosity. The amorphous regions are hypothesized to lower the thermal conductivity at faster laser scanning speeds due to less time at elevated temperatures. We also found that in-print plane and through-print plane thermal conductivities have the same value when the energy density is greater than this critical amount. When the energy density reduces below this critical amount, the in-plane conductivity exceeds the through-plane.

1. Introduction

Additive manufacturing of heat removal devices and heat exchangers is an increasingly attractive application for additive manufacturing. The material properties of parts made with additive processes are not the same as the well-established properties for bulk base materials due to the unique processes of localized heating and cooling found in additive manufacturing. For this reason, the research presented here investigates the thermal conductivity of samples produced from 316L stainless steel using the selective laser melting additive manufacturing process as a function of processing and build axis orientation.

Selective laser melting (SLM) is an additive manufacturing process that allows solid metal or plastic parts to be produced from powder. Solid metal items are produced when a laser melts and fuses metal

powder together in a layer-by-layer process [1]. In powder bed SLM, a thin layer of metal powder, typically 20–40 μm thick, is deposited over the surface of the machine's build platform and a laser is then scanned over a portion of that layer, melting the powder which subsequently solidifies [2,3]. Electro Optical Systems' (EOS) SLM printers, for example, accomplish the powder deposition by pushing powder over the build platform using a recoating blade. An alternative method for depositing the powder is by spraying it through a nozzle onto the build area as the laser melts it, commonly referred to as direct metal deposition (DMD) which is categorized under direct energy deposition process (DED) [4–6]. In both SLM and DMD, the thermal processing profiles and layer-by-layer processing are similar in terms of rapid cooling and material systems.

The SLM process continues to become more widely employed by companies for prototyping and increasingly for production. The unique

* Corresponding author.

E-mail address: sschiff@binghamton.edu (S.N. Schiffres).<https://doi.org/10.1016/j.addma.2019.100996>

Received 2 October 2019; Received in revised form 26 November 2019; Accepted 9 December 2019

Available online 13 December 2019

2214-8604/ © 2019 Published by Elsevier B.V.

capabilities of SLM enables the incorporation of features that would have been cost prohibitive or even impossible with traditional manufacturing, such as lattice structures to reduce weight or internal cooling channels to improve device cooling. A specific example of the benefits of SLM is GE's Leap fuel nozzle. By using additive manufacturing, over twenty individual parts, that were previously welded together, were SLM manufactured as a single part, leading to a 25 % reduction in its weight [7,8]. SLM is also being used by SpaceX to manufacture components for their rocket engines [9].

Depending on the process parameters used when creating parts with selective laser melting, the physical properties can vary significantly from the bulk properties of the same alloy processed conventionally [10–18]. For example, Gong observed a change in ultimate tensile strength from 1237 MPa to 978 MPa in Ti-6Al-4V specimens produced by SLM by changing the laser power and scanning speed [10]. The effect of processing parameters on thermal properties, however, has not been intensively investigated or reported for selective laser melted parts. Furthermore, how the thermal conductivity varies in a 3D printed part locally has not been previously investigated.

Printed metal heat exchangers and heat pipes have great potential to improve efficiency and reduce weight. While stainless steel is not a particularly high thermal conductivity metal, it does possess high temperature and corrosion resistance, which makes it appealing for high-temperature and corrosive environment heat transfer applications [19–22]. These thermal properties are important for many applications. For instance, additive manufacturing can reduce injection molding time per part by implementing conformal cooling. The potential to reduce the cycle time in injection molding is significant because the cooling time can be “between 60 % to as much as 90 % of the total cycle time” [23]. In this application, thermal conductivity is important, as it dictates the rate at which injection molded parts can be produced [24]. Stainless steel is often used for molds for medical applications that value smooth surfaces and with polymers that have corrosive precursors (e.g. PVC) [25].

An additional motivation for studying the thermal conductivity is the relationship between mechanical and thermal properties for enhanced non-destructive testing. Thermal properties change with micro- and nanostructure, such as the development of amorphous regions or precipitates. Because of this, probing the thermal properties has the potential to determine subtle variations in material characteristics indirectly, and could thus improve the inverse mapping of microstructure from thermal measurements for better non-destructive testing.

The thermal properties of the SLM part can vary due to the unique processing conditions, specifically the rapid cooling (e.g. $10^5 \sim 10^7$ °C/s) [26–28]. This rapid cooling could lead to non-equilibrium states that trap impurities, induce residual stresses, or generate amorphous regions. There may be unfused powder that did not wet the metal below due to an oxide film and/or processing power. Porosity is also induced from metal vaporization and powder denudation [29], which is expected to also lower thermal conductivity. There is also grain orientation anisotropy induced by the extreme thermal gradients during the melting and solidification process [30]. Therefore, the thermal properties cannot be assumed to be the same as traditional bulk materials processed by conventional means.

Previous work has shown that SLM of 316 L produces fine dendritic grains, on the scale of 1 μm , that grow parallel to each other in separate colonies [31–34]. The crystallization type has also been shown to depend on the location within the melt pool [31]. Higher energy density can cause recrystallization in the previous layer, where a lower energy density may not [31].

The dominant phase present in 316 L stainless steel produced from SLM is austenite ($\gamma\text{-Fe}$), because 316 L does not develop martensite when quickly cooled to room temperature [31–33,35]. Sigma, delta-ferrite phases, and carbide microstructures have been observed in an austenite phase matrix for stainless steel additively manufactured via arc melting and selective laser melting [34,35]. The sigma and delta-

ferrite phases can be reduced or eliminated by holding the material at temperatures above 1000 °C for one hour or more and then quenching in water [35].

Different phases and precipitates found within a metal alloy can influence its thermal conductivity. Aluminum alloys are arguably the most studied metal alloy system from a thermal conductivity perspective. Conventionally processed aluminum alloys change thermal conductivity with heat treatments due to microstructure evolution [36,37]. For aluminum alloys, Si solutes were found to impact the thermal conductivity [36]. This is because the Si initially precipitates within the inter-granular region, adding thermal interfaces. Upon heat treatment, the Si transforms to small precipitates that are less heat resistant. Similar heat treatment is not typical for 316 L and no inter-granular films form in 316 L, unlike with Al10SiMg.

While there are only a few thermal conductivity studies for additively manufactured materials [38–40], there are not any studies on the thermal conductivity of additively manufactured 316 L stainless steel. There are several relevant thermal transport studies of bulk stainless steels, sintered stainless steels, and powdered stainless steels in the literature [41–47]. These studies found the thermal conductivity of 316 L stainless steel powder before sintering ($\sim 0.1\text{--}0.3$ W/m-K). They also observed the thermal conductivity in sintered stainless steels decreased with increasing porosity [42,47].

There are no published studies on the thermal properties of laser powder-bed fusion stainless steels and none that have looked at the thermal properties versus processing or build direction. Moreover, there are currently no published results that relate local thermal conductivity variation at the microscale to the microstructure for this processing technique.

2. Material and methods

2.1. Overview

An EOS M290 selective laser melting printer was used to produce $8 \times 8 \times 1.5$ mm 316L stainless steel samples under varying laser scanning speed while the other process parameters remained at the recommended values from EOS. The samples were removed from the build platform using wire electrical discharge machining (EDM) and the two 8×8 mm faces were polished to prep for additional characterizations. The thermal conductivity and material structure of the samples were characterized by local thermal conductivity mapping, bulk thermal conductivity measurements, scanning electron microscopy, electron backscatter diffraction, x-ray diffraction, electron dispersive spectroscopy, transmission electron microscopy, and optical microscopy as a function of processing parameters and build orientation.

2.2. Selective laser melting

Powder bed selective laser melting was used to produce samples for this study. This is achieved by taking a 3D model of the part to be made and slicing it into layers. After each layer of powder is deposited, the laser scans over that layer, melting the powder and fusing it into solid metal upon cooling. The process repeats to build the model layer-by-layer. The primary processing parameters that can be adjusted are layer height, laser power, laser scanning speed, and the hatch spacing (spacing between adjacent scan lines, Fig. 1).

The important processing parameters are linked together to calculate the energy density using Eq. (1).

$$\text{Energy Density} \left[\frac{\text{J}}{\text{mm}^3} \right] = \frac{\text{Laser Power [W]}}{\text{Laser Scan Speed} \left[\frac{\text{mm}}{\text{s}} \right] \times \text{Hatch Spacing [mm]} \times \text{Layer Thickness [mm]}} \quad (1)$$

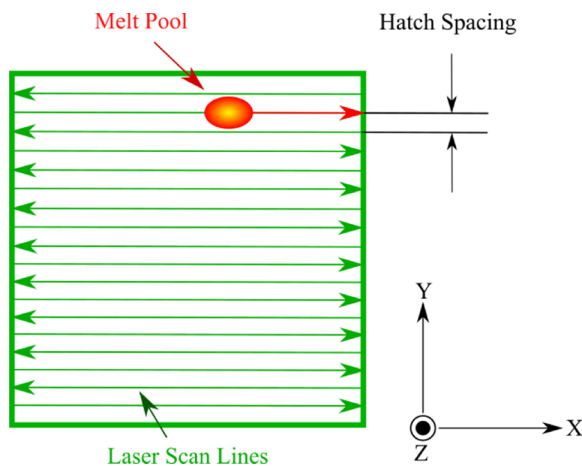


Fig. 1. Depiction of hatch spacing.

For this study, two sets of six testing specimens were produced using the EOS M290 SLM printer. The 316 L stainless steel powder was obtained from EOS [48]. The dimensions of each of the samples produced was $8 \times 8 \times 1.5$ mm and they were printed using a layer height of $40 \mu\text{m}$ and a hatch spacing of $90 \mu\text{m}$. The laser power was set to 200 W and the scanning speed was varied from 750 mm/s to 2000 mm/s in increments of 250 mm/s, representing energy densities from 74.1 J/mm^3 to 27.8 J/mm^3 . These samples were produced in two sets, one set with the 8×8 mm faces parallel to the build platform in the x-y plane and the other with the samples oriented vertically in the x-z plane. This allowed testing of thermal conductivity both through the build layers, referred to as through-plane and measured using the x-y orientation samples, and along the build layers, referred to as in-plane and measured using the x-z orientation samples. It should be noted that samples with laser scanning speeds of 250 mm/s and 500 mm/s failed to print due to splattering and warping induced by high thermal stress. No heat treatment was performed on the as-built parts, as 316 L stainless steel parts are not recommended for heat treatment by EOS due to undesirable phase transformations, like the precipitation of chromium carbides [48,49,50].

The samples were removed from the build platform by wire EDM and polished using progressively finer silicon carbide paper from 240 to 800 grit prior to flash diffusivity measurements. After the flash diffusivity testing was completed, the samples were polished further with 6-0.05 μm polishing compound prior to microscopy and testing with FDTR. The sample preparation and measurements were designed and carried out in order to eliminate the effect of geometry driven thermal history on microstructure by fabricating rectangular specimens and employing single laser exposure parameter (skin exposure) on the entire build, mechanically polishing sample surfaces and carrying out FDTR measurements at the center of the samples [51,52].

Arithmetic average roughness values (R_a) of between $10 \mu\text{m}$ – $20 \mu\text{m}$ are typical for selectively laser melted stainless steel 316 L [53,54]. Parenthetically, surface roughness enhances turbulent convective heat transfer.

2.3. Porosity and density measurement

Images of the polished surfaces of each sample were taken using a Zeiss Axio optical microscope. The images were then imported into the ImageJ software and digitized to 8-bit binary [55]. The “analyze particles function” in ImageJ was then used to determine the percentage of the area in the image made up of voids. This allowed the porosity of each sample to be approximated from these experimental images, assuming isotropic distribution of voids.

Density was calculated by multiplying the percentage of solid metal in the images by the density of the solid material given in the EOS

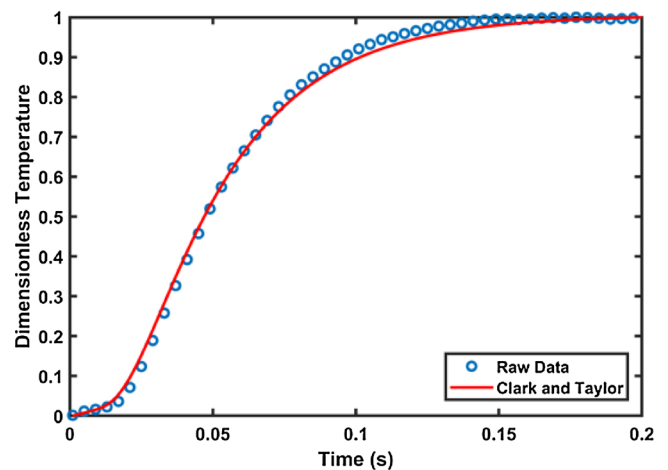


Fig. 2. Clark and Taylor model analysis of flash diffusivity data for 750 mm/s laser scanning speed sample, $k = 14.2 \text{ W/m-K}$.

datasheet [48]. The results were verified by measuring the mass of the samples, with an analytical balance, and the volume of each sample, using a Quantachrome Ultrapyc 1200e ultracycrometer, to calculate density.

2.4. Flash diffusivity

Flash diffusivity tests determine the bulk thermal diffusivity from the time-dependent temperature response of a sample exposed to a pulse of heating [56–58]. The thermal diffusivity values of the samples were determined by fitting the experimental temperature versus time data to the analytical solution of Clark and Taylor with the thermal diffusivity as the free variable [59]. An example comparison between the experimental data and the corresponding fit for the through plane, 750 mm/s laser scanning speed sample is shown in Fig. 2.

2.5. Frequency domain thermoreflectance

The local thermal conductivities of the samples were measured by frequency domain thermoreflectance (FDTR). This process works by modulating the surface temperature by focusing a modulated laser (488 nm), referred to as the pump, onto the sample surface [60]. A second co-axial laser (532 nm), referred to as the probe, is then used to sample the temperature oscillation through the change in reflectance with temperature due to the change in the top surface’s reflectance with temperature. This periodic oscillation of the reflected probe signal is sensed with a photodiode connected to a lock-in amplifier [60]. A schematic of the overall measurement process is shown in Fig. 3.

Based on the phase lag between the pump laser and the reflected probe laser, the thermal properties of the material can be determined [60,61]. The thermal conductivity of the samples were determined by fitting the phase lag vs frequency to an analytical model using MATLAB’s nonlinear regression [60,61]. An example of the phase lag data from one of the tests is shown in Fig. 4 along with the analytical fit to the data.

The spatial resolution of this technique with a 5X objective is approximately $\sim 7 \mu\text{m}$ in the x-y direction, with the laser incident on the surface traveling in the z-direction. The z-axis sensitivity can be approximated by the following equation for thermal penetration depth [60]:

$$L = \sqrt{\frac{\alpha}{\pi f}} \quad (2)$$

In this equation, L is the thermal penetration depth, α is the thermal diffusivity and f is the modulation frequency [60]. The testing for these

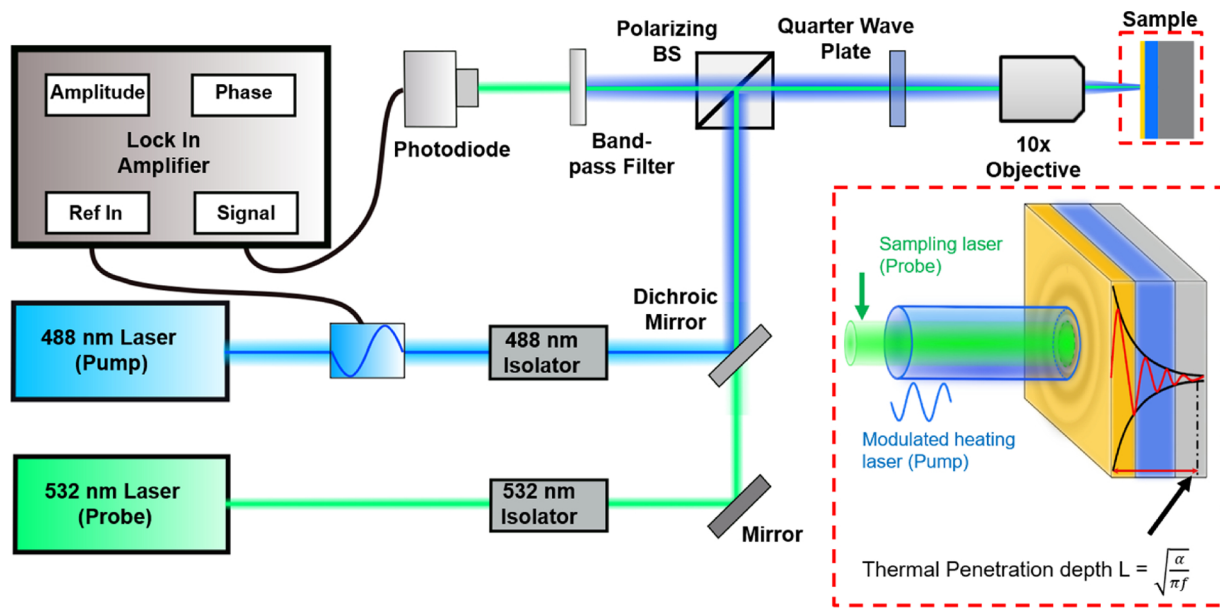


Fig. 3. Frequency domain thermorefectance experimental schematic.

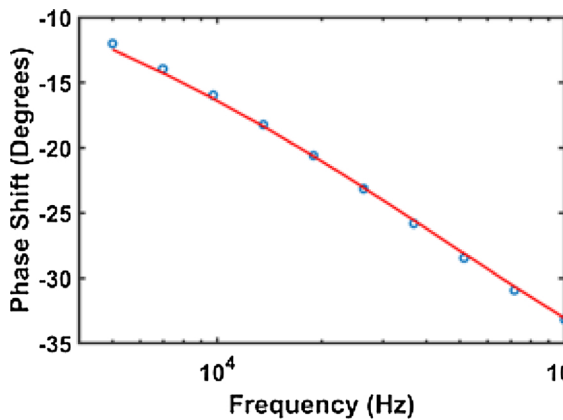


Fig. 4. 750 mm/s through-plane sample example FDTR fitting of thermal phase shift vs frequency, $k = 14.7 \text{ W/m-K}$.

samples was performed over a modulation frequency range of 5 kHz–100 kHz, which translates into a thermal penetration depth of 15.2 μm to 3.41 μm , respectively, for 316 L. Because the maximum penetration depth is less than the layer height of 40 μm , the FDTR thermal measurements are most sensitive to the through-plane samples and is unlikely to feel the effect of thermal resistances between layers.

3. Results and discussion

Fig. 5 shows the variation of average porosity with laser scanning speed. At 750 mm/s to 1250 mm/s laser scanning speed, the density remained relatively constant at about $7990 \pm 80 \text{ kg/m}^3$. The highest porosity for these samples, measured optically, was 0.40 %. As the laser scanning speed was increased past 1250 mm/s, up to 2000 mm/s, the porosity increased, up to 12.8 % at 2000 mm/s, and, in turn, caused the density to drop. The insets show representative cross-section images. (See supplemental information Fig. S1 for images taken of the polished surfaces of the six x-y orientation samples, which were used to measure the through-plane conductivity.) The 750 mm/s and 1000 mm/s samples had minimal voids, all of which were less than 25 μm in diameter. The 1250 mm/s sample had more voids, but the majority were still less than 25 μm in diameter. However, the 1500 mm/s sample showed a significant increase in the number and size of voids, with some voids

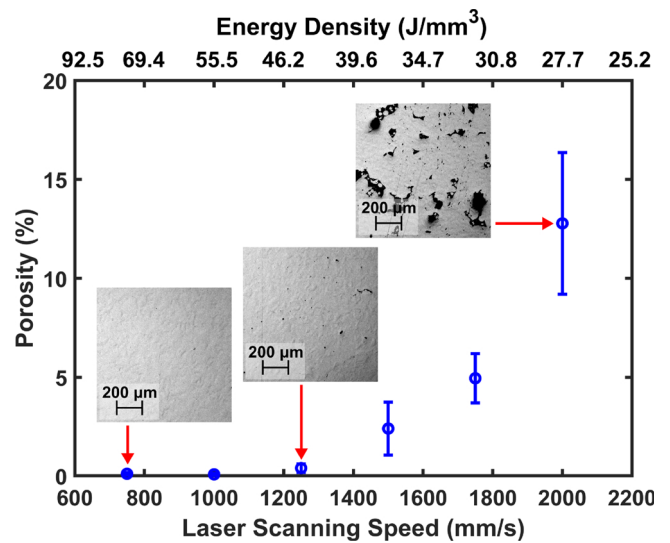


Fig. 5. Porosity vs Laser Scanning Speed. The error bars represent one standard deviation from the average measured value. The inset images are polished cross-section images that show the porosity.

being > 100 μm in diameter. At the highest laser scanning speeds (1750 mm/s to 2000 mm/s) the quantity of large voids increased significantly, with some obtaining a diameter of over 200 μm .

To investigate the microstructure of selective laser melted 316 L, tests were done using both electron backscatter diffraction (EBSD) and energy dispersive x-ray spectroscopy (EDS). These tests were done on the x-z orientation, 1000 mm/s laser scanning speed sample. This sample was chosen because the process parameters used were very close to the recommended process parameters from EOS for 316 L and the x-z orientation allows the microstructure through multiple build layers to be investigated. Almost the entire area tested was composed of austenite. There were small sections present that were not found to be austenite, but these sections had a low confidence index and appear to be due to imperfections in the polishing. Also, it was found that the concentration of alloying elements (Ni, Cr) did not vary over the surface within the spatial resolution of scanning electron microscopy electron dispersive spectroscopy (EDS) (See supplemental information Fig. S2).

In the EBSD map, the z-direction on the build platform is oriented

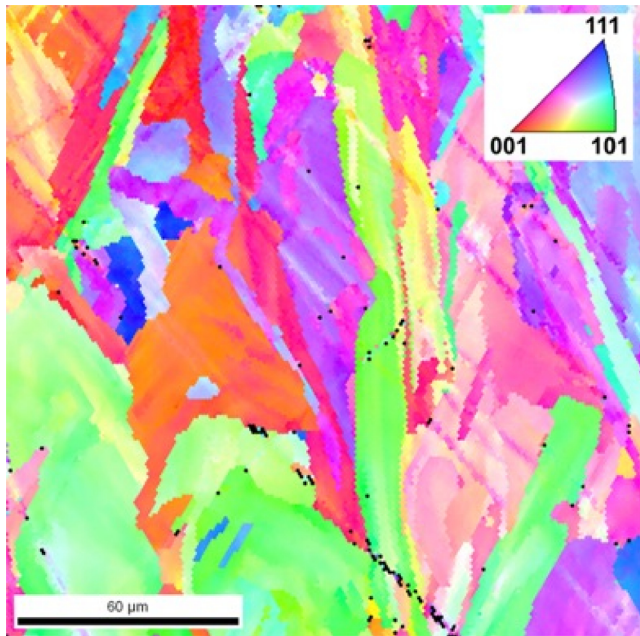


Fig. 6. Electron backscatter diffraction map of the 1000 mm/s x-z orientation 316 L sample over a $175 \times 175 \mu\text{m}$ area using an accelerating voltage of 15 kV shows the crystal structure to be entirely austenitic within the spatial resolution of this SEM technique. Grains extend through multiple layer heights.

vertically (Fig. 6). It can be seen from this image that the grains grew vertically through multiple build layers instead of being confined to individual layers, due to the grains being longer than the layer thickness of $40 \mu\text{m}$, which correlates with the microstructure data of 316 L produced by SLM from the literature [62–65]. Prior SLM literature and our TEM study show that what appears to be grains in the EBSD are actually colonies of grains with similar crystallographic orientation [28,31–34,66,67].

The thermal conductivity of each sample set shows a similar critical laser scanning speed, above which the thermal conductivity begins to reduce (Fig. 7). We also see that the conductivity in the plane of the print layer is equal to the through-plane when the laser scanning speed is below a critical value. At faster laser scanning speeds, equating to energy densities less than 44.4 J/mm^3 , the through-plane falls below the in-plane conductivities. This is due to thermal resistance between print layers impeding heat flow across layers.

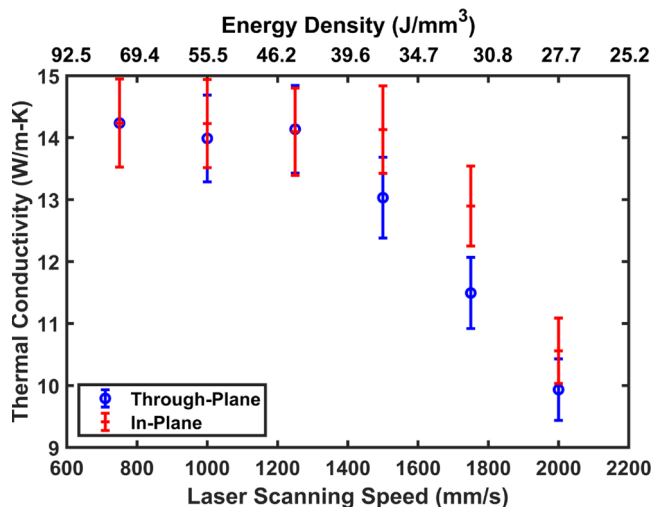


Fig. 7. Thermal conductivity of stainless steel vs laser scanning speed and energy density.

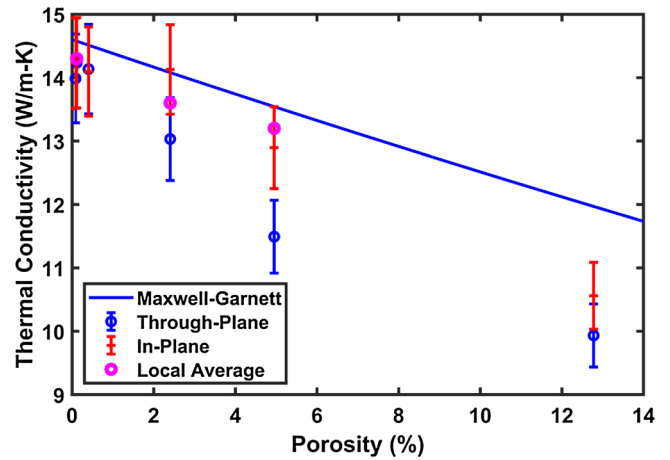


Fig. 8. Experimental and Predicted Thermal Conductivity vs Porosity. Results of flash diffusivity in-plane, through-plane, and frequency domain thermorefectance are plotted versus porosity. The Maxwell-Garnett theoretical effective medium model is plotted versus porosity.

The thermal conductivity results indicate that as the porosity increased, the thermal conductivity decreased, as expected (Fig. 8). The heat conduction through the sample is reduced, since the heat transfer through the particles and the gas making up the void space is significantly lower than the bulk solid.

We compared the thermal conductivity trend vs porosity to theoretical effective medium modeling. The Maxwell-Garnett equation, shown in Eq. (3), can also be used to predict the thermal conductivity when porosity is present, [68]

$$k_{eff} = \frac{k_m + 2k_m p \frac{k_i - k_m}{k_i + 2k_m}}{1 - p \frac{k_i - k_m}{k_i + 2k_m}} \quad (3)$$

This equation predicts the effective thermal conductivity of a composite material with a volume fraction of spherical inclusions p . Here, we assume the matrix material conductivity, k_m , is 14.6 W/m-K [69–72], and the spherical inclusion conductivity k_i is zero. Fig. 8 shows that the theoretical Maxwell-Garnett equation overpredicts the trend in thermal conductivity for SLM 316 L by about 10 % at 12.8 % porosity. This result indicates that porosity was not the only factor contributing to the reduction in conductivity. Based on Fig. 8, it can be seen that the in-plane thermal conductivity for the ~13 % porosity sample drops by 27 % compared to literature 316 L. According to the Maxwell-Garnett equation, approximately 69 % of that drop is due to the porosity, while 31 % is due to changing microstructure. Even at optimal processing, the thermal conductivity is less than literature conventionally formed 316 L by 3.4 %, while the porosity is miniscule, indicating that the thermal conductivity is not purely due to porosity.

The local variation in thermal conductivity was evaluated using frequency domain thermorefectance mapping. The map for 750 mm/s is shown in Fig. 9. A histogram of the thermal conductivity values at every point was created and is shown in the Fig. 10. The lowest value for conductivity found in the FDTR test was 10.4 W/m-K and the highest was 19.8 W/m-K , with a mean of 14.3 W/m-K . Sixty-seven percent of the points had calculated thermal conductivity values in the range of 13.0 W/m-K to 15.5 W/m-K . FDTR maps were also made for the 1500 mm/s and 1750 mm/s laser scanning speed through-plane conductivity samples. The variation in thermal conductivity does not match the crystal orientation pattern observed in EBSD (Fig. 6). No spatial elemental variation was observed with scanning electron microscopy elemental mapping using EDS (Fig. S2). For single crystal FDTR on Silicon with a $\sim 6 \mu\text{m}$ $1/e^2$ beam radii for the pump and probe, the standard deviation was less than 2 %, so these variations are significant.

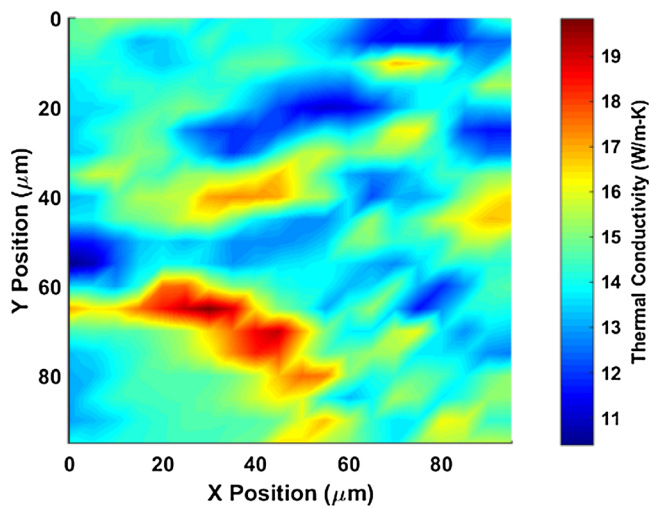


Fig. 9. Thermal Conductivity Map for 750 mm/s Through-Plane Orientation Laser Scanning Speed Sample. A 20×20 grid using a spacing of $5 \mu\text{m}$ between each position.

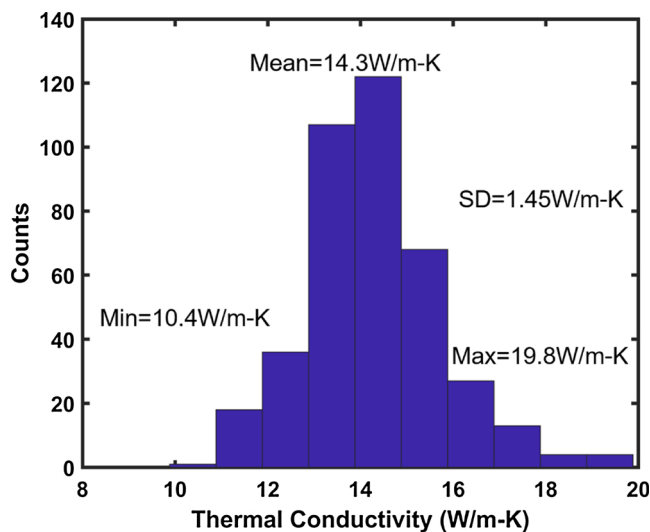


Fig. 10. Histogram of the thermal conductivity results from Fig. 9.

The average local thermal conductivity from the FDTR experiments also decreased with increasing laser scanning speed, but at a slower rate than the bulk measurements of the same samples. Because void locations were excluded from the local conductivity map calculations, the average FDTR conductivity is representative of the bulk thermal conductivity. Hence, the thermal mapping supports the conclusion drawn from the effective medium model that the bulk 316L matrix conductivity reduces above a critical laser scanning speed (or equivalently, below a critical energy density).

Transmission electron microscopy (TEM) characterization was performed using a FEI Talos F200X operating at 200 kV equipped with a four-quadrant energy dispersive X-ray spectroscopy (EDS) detector for elemental mapping. High-resolution TEM and electron diffraction analyses were performed with a JEOL 2100 microscope operating at 200 KeV. Specimens for TEM were prepared using a focused ion beam system (FEI Helios Nanolab 600 Dual Beam).

Fig. 11(a) illustrates a high-angle annular dark field (HAADF) image showing the typical morphology of the sample produced with the laser scanning speed of 2050 mm/s. The relatively low magnification HAADF image shows the grain sizes ranging from 1 to $2 \mu\text{m}$. Fig. 11(b, c) show the electron diffraction patterns obtained from two neighboring grains as marked with dashed boxes in Fig. 11(a). The diffraction patterns can

be indexed well with the face-centered cubic structure of austenitic 316 L stainless steel, consistent with the XRD results shown in Fig. 13. Fig. 11(d) is a HRTEM image obtained from a grain boundary region as marked with a solid box in Fig. 11(a). The overlapping of crystalline lattice fringes in the two grains give rise to Moiré fringes across the grain boundary area, indicating the good crystallinity in the grain boundary region. However, there are some stripe-like regions within the grains that show amorphous features with significantly reduced lattice contrast, as marked with dashed lines in Fig. 11(d). The volume fraction of the amorphous phase inside this grain is $\sim 10\%$ based on the total coverage of the amorphous regions shown in Fig. 11(d). A second type of amorphous region was identified along the grain boundary, as shown by the HAADF image in Fig. 11(e). Elemental maps show these grain boundary precipitates consist of Si, O and Mn (Fig. 11(f)).

X-ray diffraction (XRD) characterization was performed on samples printed with the same process parameters as listed above, but with laser scanning speeds ranging from 900 mm/s to 2050 mm/s. Measurements were performed on Bruker D8 Advance powder diffractometer equipped with LynxEye PSD detector using sealed X-ray tube with Cu anode and Ni β -filter. Obtained XRD patterns were fitted using Rietveld method. Scale factor from the fitting is proportional to the quantity of the phase. The results are presented in Fig. 12 and show that thermal conductivity and the XRD peak intensity share the same critical speed. Fig. 13 illustrates changes of intensity for the 111 diffraction peak.

We hypothesize that these internal amorphous striped regions are the source of lower thermal conductivity than anticipated from effective medium theory. Slower laser scanning speeds have longer thermal penetration depths, which expose the previously printed layers to a greater number of rewarming cycles, thus leading to more complete crystallization. Studies have shown materials that are normally crystalline can be produced with an amorphous structure when produced with ultrafast cooling rates [73]. Porosity does not explain the observed decrease in XRD peak intensity. This reduction in XRD intensity indicates that there are greater concentrations of amorphous regions inside the austenitic grains at faster laser scanning speeds. Hence, XRD and HR-TEM both support the hypothesis that faster laser scanning speeds lead to greater volume fraction of amorphous regions, and lower the thermal conductivity below that predicted by theoretical effective medium models.

4. Conclusion

For laser scanning speed from 750 mm/s to 1250 mm/s, the porosity remained less than 1 % and the thermal conductivity was $14.1 \pm 0.8 \text{ W/m-K}$. After the laser scanning speed was increased past the critical value, of 1250 mm/s at 200 W (energy density of 44.4 J/mm^3), the porosity increased rapidly. At the fastest laser scanning speed tested, 2000 mm/s scanning speed (energy density of 27.8 J/mm^3), incomplete fusion and the creation of voids occurred (a porosity of 12.8 %) and the bulk thermal conductivity dropped to $10.2 \pm 0.5 \text{ W/m-K}$. These results show that, like structural properties, thermal properties are also affected by process parameters in additive manufacturing. If the energy density of the process is too low, the thermal conductivity is reduced more than predicted by effective medium models. The experimental results showed thermal conductivity reduced by a third as laser scanning speed goes from 1250 mm/s to 2000 mm/s.

This study has shown that the unique thermal profile of SLM changes the microstructure relative to traditionally processed materials and alters the thermal conductivity locally of additively manufactured 316L stainless steel. When the processing conditions employ lower energy densities than optimum, the bulk thermal conductivities are below the theoretical effective medium thermal conductivity prediction by as much as 10 % [47].

This reduction below the model predictions is theorized to be due to

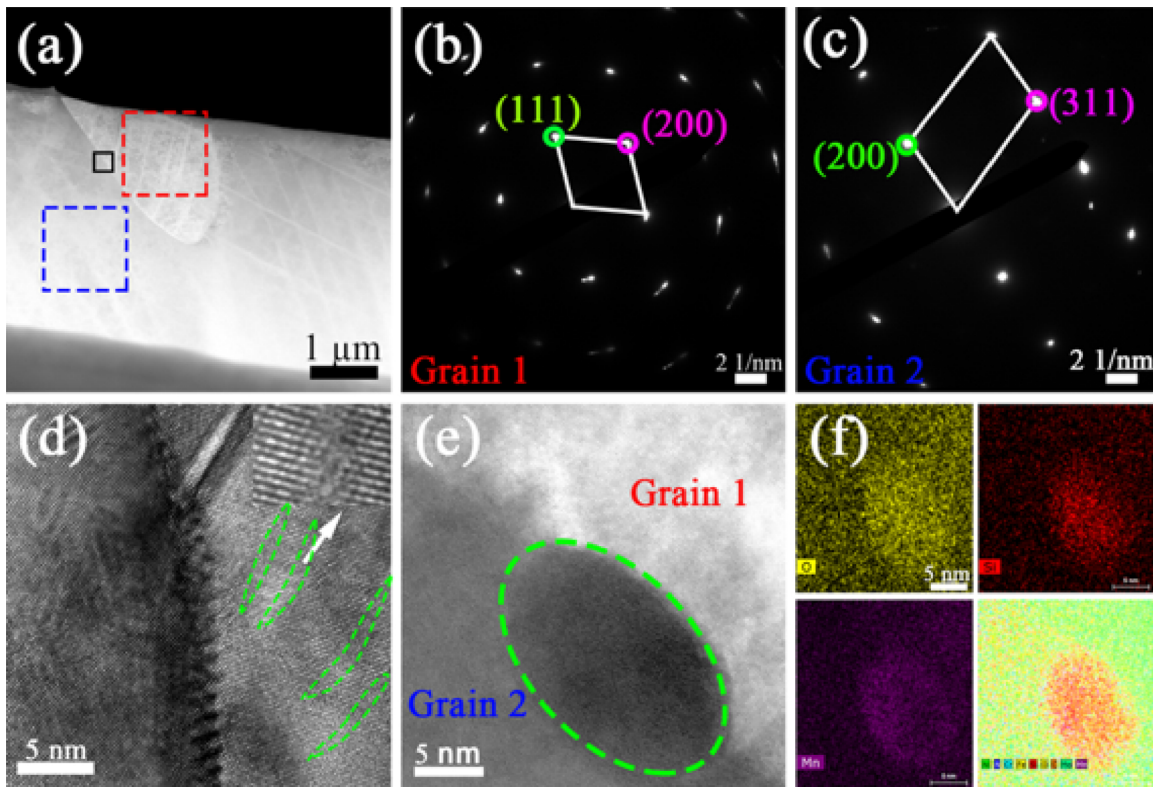


Fig. 11. TEM characterization of the sample produced with the laser scanning speed of 2050 mm/s. (a) HAADF micrograph showing the typical morphology. (b, c) selected area electron diffraction patterns from two neighboring grains marked with dashed boxes b and c in (a). (d) HRTEM image obtained from the grain boundary area marked with box d in (a). (e) HAADF image showing grain boundary precipitation in the area marked with the solid box in (a). (f) EDS maps of the grain boundary precipitate shown in (e).

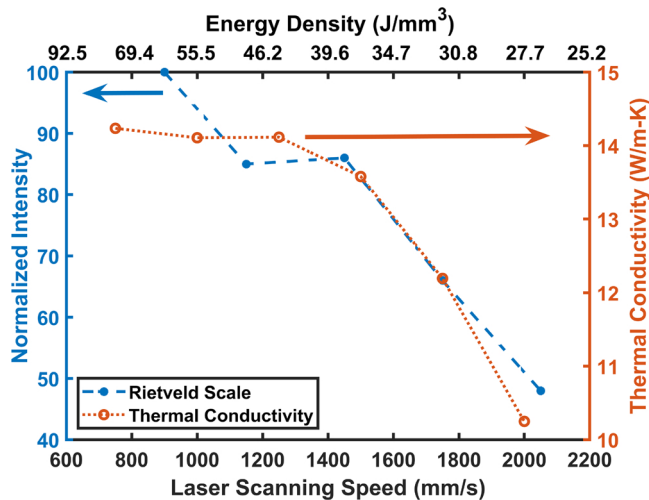


Fig. 12. XRD Peak Intensity (Rietveld Scale) and Thermal Conductivity versus Laser Scanning Speed.

amorphous regions in the material, which were observed with high resolution transmission electron microscopy as disordered stripes inside the austenite grains. This finding is also supported by the reduction in austenite x-ray diffraction peaks with increasing laser scanning speed. The development of amorphous regions can result from rapid cooling and reduced time above the recrystallization temperature. Since amorphous disorder reduces the mean free path of the electron carriers, thermal conductivity is reduced. This supports our observation of average thermal conductivity decreasing with increasing laser scanning speed. The crystallographic orientations derived from scanning electron microscopy electron backscatter diffraction maps did not indicate any

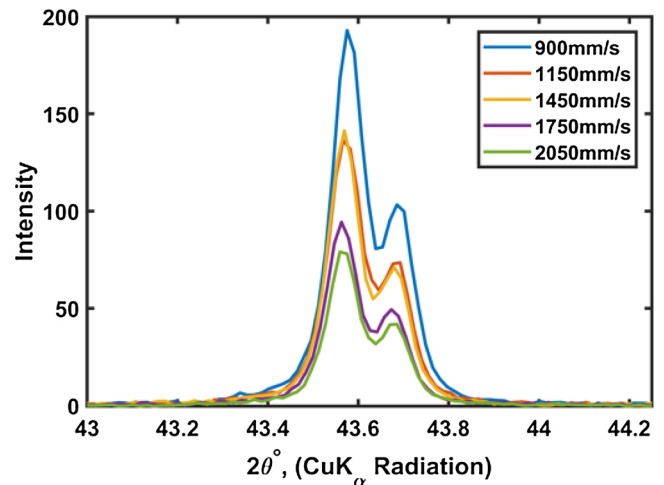


Fig. 13. Superposition of 111 diffraction peaks.

crystallographic dependence on thermal conductivity within our thermal conductivity measurement resolution.

These findings also have an impact in non-destructive testing for additive manufacturing [74,75]. Thermal conductivity is an indirect way to examine the micro- and nano-structure. The thermal properties can be probed by periodic examination of the just-printed layer using the printing laser itself [76].

Author contributions

S.N.S. conceived the initial idea of this research and guided the work. J.C.S. performed thermophysical measurements (FDTR, Flash

diffusivity) and analysis. A.A. developed the SLM processing technique and performed EBSD and EDS characterizations and analysis. M.A.D. developed the FDTR Mapping Setup and contributed towards FDTR thermal measurements. P.Y.Z analyzed the samples using XRD. X.C. and G.Z. contributed TEM characterization and analysis. All authors contributed to the writing of this paper.

Declaration of Competing Interest

The authors declare that they have no known competing financial interests or personal relationships that could have appeared to influence the work reported in this paper.

Acknowledgments

We thank Scott Volk and Shawn Wagoner of Incodema3D for their valuable advice. S.N.S gratefully acknowledges the support of NSF-1846157, SUNY Binghamton, and the ADL's Small Grant (ADLG173). J.S. and M.D. acknowledge NSF-1742056, and S.N.S. and M.D. acknowledge NSF-1846157. X.C. and G.Z. acknowledge the support by the U.S. Department of Energy, Office of Basic Energy Sciences, Division of Materials Science and Engineering under award no. DE-SC0001135. This research used resources of the Center for Functional Nanomaterials, which is a U.S. DOE Office of Science Facility, at Brookhaven National Laboratory under contract no. DE-SC0012704.

Appendix A. Supplementary data

Supplementary material related to this article can be found, in the online version, at doi:<https://doi.org/10.1016/j.addma.2019.100996>.

References

- C.Y. Yap, C.K. Chua, Z.L. Dong, Z.H. Liu, D.Q. Zhang, L.E. Loh, S.L. Sing, Review of selective laser melting: materials and applications, *Appl. Phys. Rev.* 2 (2015) 041101, <https://doi.org/10.1063/1.4935926>.
- W.E. Frazier, Metal additive manufacturing: a review, *J. Mater. Eng. Perform.* 23 (2014) 1917–1928, <https://doi.org/10.1007/s11665-014-0958-z>.
- S. Sun, M. Brandt, M. Easton, Powder bed fusion processes, *Laser Additive Manufacturing*, Elsevier, 2017, pp. 55–77, <https://doi.org/10.1016/B978-0-08-100433-3.00002-6>.
- J. Mazumder, D. Dutta, N. Kikuchi, A. Ghosh, Closed loop direct metal deposition: art to part, *Opt. Lasers Eng.* 34 (2000) 397–414, [https://doi.org/10.1016/S0143-8166\(00\)00072-5](https://doi.org/10.1016/S0143-8166(00)00072-5).
- S. Bhattacharya, G.P. Dinda, A.K. Dasgupta, J. Mazumder, Microstructural evolution of AISI 4340 steel during Direct Metal Deposition process, *Mater. Sci. Eng. A* 528 (2011) 2309–2318, <https://doi.org/10.1016/j.msea.2010.11.036>.
- ISO/ASTM 52900:2015(en), Additive manufacturing — General principles — Terminology, (n.d.). <https://www.iso.org/obp/ui/#iso:std:iso-astm:52900:ed-1:vi:en> (Accessed November 11, 2019).
- T. Kellner, How 3D Printing Will Change Manufacturing, *GE Reports*, (2017) (Accessed June 30, 2018), <https://www.ge.com/reports/epiphany-disruption-ge-additive-chief-explains-3d-printing-will-upend-manufacturing/>.
- New manufacturing milestone: 30,000 additive fuel nozzles, *GE Additive*. (n.d.). <https://www.ge.com/additive/blog/new-manufacturing-milestone-30000-additive-fuel-nozzles> (Accessed April 22, 2019).
- H. Post, SpaceX Launches 3D-Printed Part to Space, Creates Printed Engine Chamber, *SpaceX*, (2014) (Accessed June 30, 2018), <http://www.spacex.com/news/2014/07/31/spacex-launches-3d-printed-part-space-creates-printed-engine-chamber-crewed>.
- H. Gong, Generation and Detection of Defects in Metallic Parts Fabricated by Selective Laser Melting and Electron Beam Melting and Their Effects on Mechanical Properties, (2013) (Accessed September 30, 2017), <http://ir.library.louisville.edu/etd/515/>.
- M. Yakout, M.A. Elbestawi, S.C. Veldhuis, On the characterization of stainless steel 316L parts produced by selective laser melting, *Int. J. Adv. Manuf. Technol.* 95 (2018) 1953–1974, <https://doi.org/10.1007/s00170-017-1303-0>.
- M. Yakout, M.A. Elbestawi, S.C. Veldhuis, Density and mechanical properties in selective laser melting of Invar 36 and stainless steel 316L, *J. Mater. Process. Technol.* 266 (2019) 397–420, <https://doi.org/10.1016/j.jmatprotec.2018.11.006>.
- J. Gockel, J. Beuth, K. Taminger, Integrated control of solidification microstructure and melt pool dimensions in electron beam wire feed additive manufacturing of Ti-6Al-4V, *Addit. Manuf.* 1–4 (2014) 119–126, <https://doi.org/10.1016/j.addma.2014.09.004>.
- J. Beuth, N. Klingbeil, The role of process variables in laser-based direct metal solid freeform fabrication, *JOM* 53 (2001) 36–39, <https://doi.org/10.1007/s11837-001-0067-y>.
- M. Tang, P.C. Pistorius, J.L. Beuth, Prediction of lack-of-fusion porosity for powder bed fusion, *Addit. Manuf.* 14 (2017) 39–48, <https://doi.org/10.1016/j.addma.2016.12.001>.
- Y. He, C. Montgomery, J. Beuth, B. Webler, Melt pool geometry and microstructure of Ti6Al4V with B additions processed by selective laser melting additive manufacturing, *Mater. Des.* 183 (2019) 108126, <https://doi.org/10.1016/j.matdes.2019.108126>.
- C. Montgomery, J. Beuth, L. Sheridan, N. Klingbeil, Process mapping of inconel 625 in laser powder bed additive manufacturing, *Proceedings of the 2015 Solid Freeform Fabrication Symposium*, Austin, TX, 2015, p. 10.
- C. Montgomery, C. Farnin, G. Mellos, M. Brand, R. Pacheco, J. Carpenter, Effect of shield gas on surface finish of laser powder bed produced parts, *Proceedings of the 2018 Solid Freeform Fabrication Symposium*, Austin, TX, 2018, p. 7 <http://sffsymposium.engr.utexas.edu/sites/default/files/2018/03/7%20EffectofShieldGasOnSurfaceFinishofLaserPo.pdf>.
- The Role of Stainless Steels in Industrial Heat Exchangers, *Nickel Institute*. (n.d.). https://www.nickelinstitute.org/media/1783/roleofstainlesssteelsinindustrialheatexchangers_9005_.pdf (Accessed March 29, 2019).
- P. Rodriguez, Selection of Materials for Heat Exchangers (n.d.), (2019), p. 14.
- H.-M. Lee, M.-C. Tsai, H.-L. Chen, H.-Y. Li, Stainless steel heat pipe fabrication, performance testing and modeling, *Energy Procedia* 105 (2017) 4745–4750, <https://doi.org/10.1016/j.egypro.2017.03.1032>.
- D. O. Silva, R.R. Riehl, Thermal behavior of water-copper and water-stainless steel heat pipes operating in cycles, 2016 15th IEEE Intersociety Conference on Thermal and Thermomechanical Phenomena in Electronic Systems (ITherm) (2016) 6–11, <https://doi.org/10.1109/ITHERM.2016.7517521>.
- V. Brøtan, O.Å. Berg, K. Sørby, Additive manufacturing for enhanced performance of molds, *Procedia Cirp* 54 (2016) 186–190, <https://doi.org/10.1016/j.procir.2016.05.074>.
- S. Kalpakjian, S. Schmid, *Manufacturing Engineering & Technology*, 7th ed., Pearson, 2014.
- TOOLING: How to Select the Right Tool Steel for Mold Cavities, (2019) (n.d.). <https://www.ptonline.com/columns/tooling-how-to-select-the-right-tool-steel-for-mold-cavities> (accessed March 28, 2019).
- S. Pauly, P. Wang, U. Kühn, K. Kosiba, Experimental determination of cooling rates in selectively laser-melted eutectic Al-33Cu, *Addit. Manuf.* 22 (2018) 753–757, <https://doi.org/10.1016/j.addma.2018.05.034>.
- D. Buchbinder, H. Schleifenbaum, S. Heidrich, W. Meiners, J. Bültmann, High power selective laser melting (HP SLM) of aluminum parts, *Phys. Procedia* 12 (2011) 271–278, <https://doi.org/10.1016/j.phpro.2011.03.035>.
- Z. Sun, X. Tan, S.B. Tor, W.Y. Yeong, Selective laser melting of stainless steel 316L with low porosity and high build rates, *Mater. Des.* 104 (2016) 197–204, <https://doi.org/10.1016/j.matdes.2016.05.035>.
- M.J. Matthews, G. Guss, S.A. Khairallah, A.M. Rubenchik, P.J. Depond, W.E. King, Denudation of metal powder layers in laser powder bed fusion processes, *Acta Mater.* 114 (2016) 33–42, <https://doi.org/10.1016/j.actamat.2016.05.017>.
- T. Niendorf, S. Leuders, A. Riemer, H.A. Richard, T. Tröster, D. Schwarze, Highly anisotropic steel processed by selective laser melting, *Metall. Mater. Trans. B* 44 (2013) 794–796, <https://doi.org/10.1007/s11663-013-9875-z>.
- D. Wang, C. Song, Y. Yang, Y. Bai, Investigation of crystal growth mechanism during selective laser melting and mechanical property characterization of 316L stainless steel parts, *Mater. Des.* 100 (2016) 291–299, <https://doi.org/10.1016/j.matdes.2016.03.111>.
- P. Krakhmalev, I. Yadroitsava, G. Fredriksson, I. Yadroitsev, Microstructure of SLM manufactured 316L and 420 grades stainless steel, *Proceeding of the RAPDASA 15th Annual International Conference*, 2014 November 6–7; Stellenbosch, South Africa, 2014, pp. 59–66.
- E. Liverani, S. Toschi, L. Ceschini, A. Fortunato, Effect of selective laser melting (SLM) process parameters on microstructure and mechanical properties of 316L austenitic stainless steel, *J. Mater. Process. Technol.* 249 (2017) 255–263, <https://doi.org/10.1016/j.jmatprotec.2017.05.042>.
- T. Kurzynowski, K. Gruber, W. Stopyra, B. Kuźnicka, E. Chlebus, Correlation between process parameters, microstructure and properties of 316 L stainless steel processed by selective laser melting, *Mater. Sci. Eng. A* 718 (2018) 64–73, <https://doi.org/10.1016/j.msea.2018.01.103>.
- X. Chen, J. Li, X. Cheng, H. Wang, Z. Huang, Effect of heat treatment on microstructure, mechanical and corrosion properties of austenitic stainless steel 316L using arc additive manufacturing, *Mater. Sci. Eng. A* 715 (2018) 307–314, <https://doi.org/10.1016/j.msea.2017.10.002>.
- M. Payandeh, E. Sjölander, A.E.W. Jarfors, M. Wessén, Influence of microstructure and heat treatment on thermal conductivity of rheocast and liquid die cast Al-6Si-2Cu-Zn alloy, *Int. J. Cast Met. Res.* 29 (2016) 202–213, <https://doi.org/10.1080/13640461.2015.1125990>.
- J.K. Chen, H.Y. Hung, C.F. Wang, N.K. Tang, Effects of casting and heat treatment processes on the thermal conductivity of an Al-Si-Cu-Fe-Zn alloy, *Int. J. Heat Mass Transf.* 105 (2017) 189–195, <https://doi.org/10.1016/j.ijheatmasstransfer.2016.09.090>.
- J. Simmons, A. Azizi, M. Daeumer, S. Schifres, Laser powder bed fusion processing parameters influence on thermal properties, *Solid Freeform Fabrication Symposium, Solid Freeform Fabrication Symposium*, Austin, TX, 2018, pp. 1–14.
- A. Azizi, M.A. Daeumer, S.N. Schifres, Additive laser metal deposition on Silicon, *Addit. Manuf.* (2018), <https://doi.org/10.1016/j.addma.2018.09.027>.
- H. Zhang, D. Hobbs, G.S. Nolas, S. LeBlanc, Laser additive manufacturing of

- powdered bismuth telluride, *J. Mater. Res.* 33 (2018) 4031–4039, <https://doi.org/10.1557/jmr.2018.390>.
- [41] C.Y. Ho, T.K. Chu, *Electrical Resistivity and Thermal Conductivity of Nine Selected AISI Stainless Steels*, Thermophysical and Electronic Properties Information Analysis Center Lafayette In, 1977.
- [42] W.M. Lima, V. Biondo, W.R. Weinand, E.S. Nogueira, A.N. Medina, M.L. Baesso, A.C. Bento, The effect of porosity on thermal properties: towards a threshold of particle contact in sintered stainless steel, *J. Phys. Condens. Matter* 17 (2005) 1239–1249, <https://doi.org/10.1088/0953-8984/17/7/016>.
- [43] Stainless Steel - Grade 316L (UNS S31603), AZoM.Com, 2004 (Accessed July 3, 2018), <https://www.azom.com/article.aspx?ArticleID=2382>.
- [44] J.C.Y. Koh, A. Fortini, Prediction of thermal conductivity and electrical resistivity of porous metallic materials, *Int. J. Heat Mass Transf.* 16 (1973) 2013–2022, [https://doi.org/10.1016/0017-9310\(73\)90104-X](https://doi.org/10.1016/0017-9310(73)90104-X).
- [45] M.R. Alkharri, T. Furumoto, T. Ueda, A. Hosokawa, R. Tanaka, A. Aziz, M. Sanusi, Thermal conductivity of metal powder and consolidated material fabricated via selective laser melting, *Key Engineering Materials*, Trans Tech Publ, 2012, pp. 244–249 (Accessed September 29, 2017), <https://www.scientific.net/KEM.523-524.244>.
- [46] L.C. Wei, L.E. Ehrlich, M.J. Powell-Palm, C. Montgomery, J. Beuth, J.A. Malen, Thermal conductivity of metal powders for powder bed additive manufacturing, *Addit. Manuf.* 21 (2018) 201–208, <https://doi.org/10.1016/j.addma.2018.02.002>.
- [47] J.C.Y. Koh, A. Fortini, *Thermal Conductivity and Electrical Resistivity of Porous Material*, (1971).
- [48] EOS StainlessSteel 316L Material Data Sheet EOSINT M 280 and EOS M 290, EOS GmbH - Electro Optical Systems, 2014, <https://cdn0.scrvt.com/eos/77d285f20ed6ae89/dd6850c010d3/EOSStainlessSteel316L.pdf>.
- [49] A01 Committee, Specification for Wrought Austenitic Stainless Steel Piping Fittings, ASTM International, 2019, https://doi.org/10.1520/A0403_A0403M-19 n.d..
- [50] Heat Treatment Austenitic Corrosion-Resistant Steel Parts AMS2759/4D, (2018), <https://doi.org/10.4271/AMS2759/4D>.
- [51] S. Anandan, R.M. Hussein, M. Spratt, J. Newkirk, K. Chandrashekhara, H. Misak, M. Walker, Failure in metal honeycombs manufactured by selective laser melting of 304 L stainless steel under compression, *Virtual Phys. Prototyp.* 14 (2019) 114–122, <https://doi.org/10.1080/17452759.2018.1531336>.
- [52] W.H. Yu, S.L. Sing, C.K. Chua, C.N. Kuo, X.L. Tian, Particle-reinforced metal matrix nanocomposites fabricated by selective laser melting: a state of the art review, *Prog. Mater. Sci.* 104 (2019) 330–379, <https://doi.org/10.1016/j.pmatsci.2019.04.006>.
- [53] E. Yasa, J.-P. Kruth, Microstructural investigation of Selective Laser Melting 316L stainless steel parts exposed to laser re-melting, *Procedia Eng.* 19 (2011) 389–395, <https://doi.org/10.1016/j.proeng.2011.11.130>.
- [54] Y. Sun, R. Bailey, A. Moroz, Surface finish and properties enhancement of selective laser melted 316L stainless steel by surface mechanical attrition treatment, *Surf. Coat. Technol.* (2019) 124993, <https://doi.org/10.1016/j.surfcoat.2019.124993>.
- [55] ImageJ, (n.d.). <https://imagej.nih.gov/ij/> (Accessed April 22, 2019).
- [56] Stainless Steel - Grade 316L - Properties, Fabrication and Applications (UNS S31603), AZoM.Com, 2004 (Accessed October 18, 2017), <https://www.azom.com/article.aspx?ArticleID=2382>.
- [57] Flash Diffusivity Method: A Survey of Capabilities, Electronics Cooling, 2002 (Accessed June 30, 2018), <https://www.electronics-cooling.com/2002/05/flash-diffusivity-method-a-survey-of-capabilities/>.
- [58] W.J. Parker, R.J. Jenkins, C.P. Butler, G.L. Abbott, Flash method of determining thermal diffusivity, heat capacity, and thermal conductivity, *J. Appl. Phys.* 32 (1961) 1679–1684, <https://doi.org/10.1063/1.1728417>.
- [59] L.M. Clark III, R.E. Taylor, Radiation loss in the flash method for thermal diffusivity, *J. Appl. Phys.* 46 (1975) 714–719, <https://doi.org/10.1063/1.321635>.
- [60] A.J. Schmidt, Optical Characterization of Thermal Transport from the Nanoscale to the Macroscale, Massachusetts Institute of Technology, 2008 (Accessed September 18, 2017), <https://dspace.mit.edu/handle/1721.1/44798>.
- [61] D. Cahill, Analysis of heat flow in layered structures for time-domain thermoreflectance, *Rev. Sci. Instrum.* 75 (2005) 5119–5122, <https://doi.org/10.1063/1.1819431>.
- [62] M.L. Montero-Sistiaga, M. Godino-Martinez, K. Boschmans, J.-P. Kruth, J. Van Humbeeck, K. Vanmeensel, Microstructure evolution of 316L produced by HP-SLM (high power selective laser melting), *Addit. Manuf.* 23 (2018) 402–410, <https://doi.org/10.1016/j.addma.2018.08.028>.
- [63] R. Casati, J. Lemke, M. Vedani, Microstructure and fracture behavior of 316L austenitic stainless steel produced by selective laser melting, *J. Mater. Sci. Technol.* 32 (2016) 738–744, <https://doi.org/10.1016/j.jmst.2016.06.016>.
- [64] X. Wang, J.A. Muñoz-Lerma, O. Sánchez-Mata, M. Attarian Shandiz, M. Brochu, Microstructure and mechanical properties of stainless steel 316L vertical struts manufactured by laser powder bed fusion process, *Mater. Sci. Eng. A* 736 (2018) 27–40, <https://doi.org/10.1016/j.msea.2018.08.069>.
- [65] J.H.K. Tan, S.L. Sing, W.Y. Yeong, Microstructure modelling for metallic additive manufacturing: a review, *Virtual Phys. Prototyp.* (2019) 1–19, <https://doi.org/10.1080/17452759.2019.1677345>.
- [66] C. Qiu, M.A. Kindi, A.S. Aladawi, I.A. Hatmi, A comprehensive study on microstructure and tensile behaviour of a selectively laser melted stainless steel, *Sci. Rep.* 8 (2018) 7785, <https://doi.org/10.1038/s41598-018-26136-7>.
- [67] Y.M. Wang, T. Voisin, J.T. McKeown, J. Ye, N.P. Calta, Z. Li, Z. Zeng, Y. Zhang, W. Chen, T.T. Roehling, R.T. Ott, M.K. Santala, P.J. Depond, M.J. Matthews, A.V. Hamza, T. Zhu, Additively manufactured hierarchical stainless steels with high strength and ductility, *Nat. Mater.* 17 (2017) 63–71, <https://doi.org/10.1038/nmat5021>.
- [68] V.A. Markel, Introduction to the Maxwell Garnett approximation: tutorial, *J. Opt. Soc. Am. A* 33 (2016) 1244, <https://doi.org/10.1364/JOSAA.33.001244>.
- [69] J.C. Outeiro, D. Umbrello, R. M'Saoubi, Experimental and numerical modelling of the residual stresses induced in orthogonal cutting of AISI 316L steel, *Int. J. Mach. Tools Manuf.* 46 (2006) 1786–1794, <https://doi.org/10.1016/j.ijmachtools.2005.11.013>.
- [70] L. Bodelot, L. Sabatier, E. Charkaluk, P. Dufrenoy, Experimental setup for fully coupled kinematic and thermal measurements at the microstructure scale of an AISI 316L steel, *Mater. Sci. Eng. A* 501 (2009) 52–60, <https://doi.org/10.1016/j.msea.2008.09.053>.
- [71] J. Song, J.C. Gelin, T. Barrière, B. Liu, Experiments and numerical modelling of solid state sintering for 316L stainless steel components, *J. Mater. Process. Technol.* 177 (2006) 352–355, <https://doi.org/10.1016/j.jmatprot.2006.04.111>.
- [72] C. Bonnet, F. Valiorgue, J. Rech, C. Claudin, H. Hamdi, J.M. Bergheau, P. Gilles, Identification of a friction model—Application to the context of dry cutting of an AISI 316L austenitic stainless steel with a TiN coated carbide tool, *Int. J. Mach. Tools Manuf.* 48 (2008) 1211–1223, <https://doi.org/10.1016/j.ijmachtools.2008.03.011>.
- [73] L. Zhong, J. Wang, H. Sheng, Z. Zhang, S.X. Mao, Formation of monatomic metallic glasses through ultrafast liquid quenching, *Nature* 512 (2014) 177–180, <https://doi.org/10.1038/nature13617>.
- [74] M. Seifi, A. Salem, J. Beuth, O. Harrysson, J.J. Lewandowski, Overview of materials qualification needs for metal additive manufacturing, *JOM* 68 (2016) 747–764, <https://doi.org/10.1007/s11837-015-1810-0>.
- [75] M. Grasso, B.M. Colosimo, Process defects and in situ monitoring methods in metal powder bed fusion: a review, *Meas. Sci. Technol.* 28 (2017) 044005, <https://doi.org/10.1088/1361-6501/aa5c4f>.
- [76] S.N. Schifres, M. Daeumer, J.C. Simmons, A. Azizi, ENHANCED NON-DESTRUCTIVE TESTING IN DIRECTED ENERGY MATERIAL PROCESSING, USPTO Provisional Application 62/836,064, 2019.